Research Article | Open Access

Soft Science

Yang *et al. Soft Sci.* **2026**, *6*, 97 **DOI:**10.20517/ss.2026.183

Interfacially integrated Janus bilayer hydrogel for spatially decoupled wet adhesion and hydrated lubrication

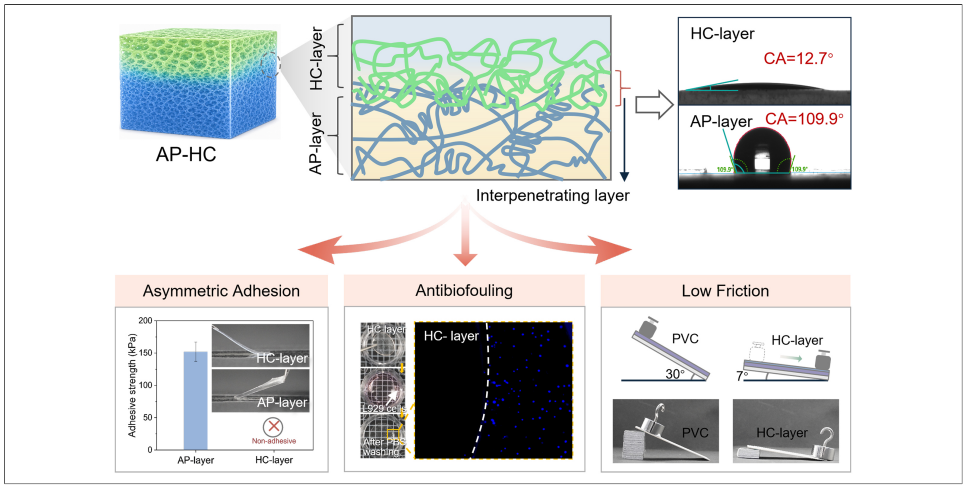
Xin Yang[1,2,#], Yuqi Wang[2,#], Yanjing Zhang[2], Zizhou Xu[2], Chaoyi Yang[2], Jianwei Ye[2], Yizhan Zhu[2], Yulin Hu[3], Shuaijun Guo[2], Shilei Zhu[2,*], Haihua Wang[1,4,*], Ya Nan Ye[2,5,*]

Keywords:
Janus hydrogel, wet adhesion, hydrated lubrication, interfacial integration, biointerface design

Citation: Yang, X.; Wang, Y.; Zhang, Y.; Xu, Z.; Yang, C.; Ye, J.; Zhu, Y.; Hu, Y.; Guo, S.; Zhu, S.; Wang, H.; Ye, Y. N. Interfacially integrated Janus bilayer hydrogel for spatially decoupled wet adhesion and hydrated lubrication. *Soft Sci.* **2026**, *6*, 97. https://dx.doi.org/10.20517/ss.2026.183

Received: 8 Jul 2026
First Decision: 24 Jul 2026
Revised: 3 Sep 2026
Accepted: 3 Sep 2026
Published: 20 Oct 2026

Academic Editors:
YongAn Huang, Jun Chen
Copy Editor:
Pei-Yun Wang
Production Editor:
Pei-Yun Wang



Abstract

Wet biointerfaces require both robust interfacial adhesion and persistent surface hydration, yet these competing functions are difficult to reconcile within a homogeneous hydrogel network. Here, we develop a molecularly integrated Janus AP-HC bilayer hydrogel to spatially decouple these competing functions. In this architecture, a mechanically robust adhesive layer (AP) provides strong and reusable wet adhesion to diverse substrates, whereas the opposing hydrated lubricating layer (HC) provides durable lubrication and suppresses bioadhesion. The two functionally distinct layers are integrated through precursor infiltration and topological entanglement: the water-rich HC precursor locally swells the pre-equilibrated AP surface to promote macromolecular interdiffusion, followed by *in situ* Schiff-base crosslinking that stabilizes the interpenetrated chains and forms a continuous transition zone. The separately prepared AP-2 hydrogel exhibits a lap-shear

[1]Shaanxi Key Laboratory of Chemical Additives for Industry, Xi'an Key Laboratory of Advanced Performance Materials and Polymers, College of Chemistry and Chemical Engineering, Shaanxi University of Science and Technology, Xi'an 710021, Shaanxi, China.
[2]College of Materials Science & Engineering, Taiyuan University of Technology, Taiyuan 030024, Shanxi, China.
[3]Department of Biomedical Engineering, College of Artificial Intelligence, Taiyuan University of Technology, Taiyuan 030024, Shanxi, China.
[4]College of Chemistry, Chemical Engineering and Materials Science, Soochow University, Suzhou 215123, Jiangsu, China.
[5]National Synchrotron Radiation Laboratory, Anhui Provincial Engineering Research Center for Advanced Functional Polymer Films, University of Science and Technology of China, Hefei 230029, Anhui, China.

***Correspondence to:** Dr. Shilei Zhu, College of Materials Science & Engineering, Taiyuan University of Technology, Taiyuan 030024, Shanxi, China. E-mail: zhushilei@tyut.edu.cn; Prof. Haihua Wang, Shaanxi Key Laboratory of Chemical Additives for Industry, Xi'an Key Laboratory of Advanced Performance Materials and Polymers, College of Chemistry and Chemical Engineering, Shaanxi University of

Science and Technology, Xi'an 710021, Shaanxi, China. E-mail: whh@sust.edu.cn; Prof. Ya Nan Ye, National Synchrotron Radiation Laboratory, Anhui Provincial Engineering Research Center for Advanced Functional Polymer Films, University of Science and Technology of China, Hefei 230029, Anhui, China. E-mail: yeyanan@ustc.edu.cn

strength of 154.6 ± 11.9 kPa on PVC substrates and retains 82.9% of its initial adhesion strength after 50 adhesion cycles. In contrast, the HC layer maintains stable low-friction lubrication under physiologically relevant conditions and effectively suppresses protein adsorption and cell adhesion. Meanwhile, the integrated AP-HC bilayer maintains interfacial and functional-layer stability under ultrasonic treatment and cyclic deformation. This spatial functional decoupling strategy provides a generalizable framework for engineering multifunctional wet biointerfaces for implantable devices and flexible bioelectronics.

INTRODUCTION

Hydrogel interfaces, by virtue of their high hydration, tissue-compatible mechanical compliance, and tunable surface chemistry, have become foundational materials for constructing wet biointerfaces in implantable devices, flexible bioelectronics, and tissue engineering[1-3]. As the frontline layer that directly couples a synthetic material with a biological environment, the hydrogel interface must simultaneously mediate mechanical transmission, resist interfacial friction, and defend against nonspecific adhesion of proteins, cells, and microorganisms during long-term service[4-6]. Consequently, hydrogel interface design has evolved beyond optimizing single attributes into a multidimensional challenge that demands concurrent, spatially organized functions.

Central to this challenge is that the physicochemical requirements for robust wet adhesion and for effective lubrication/antifouling are fundamentally opposed. Strong wet adhesion requires disruption or displacement of the interfacial water layer, intimate substrate contact, and effective interfacial bonding through hydrogen bonding, electrostatic interactions, hydrophobic interactions, or dynamic/covalent linkages[7-10]; the bulk network must also possess sufficient cohesion and energy-dissipation capacity to resist peeling and shear loading[11-13]. In contrast, lubricating and antifouling surfaces rely on stable surface hydration layers that suppress nonspecific protein, cell, and microbial adhesion[14-16]. Thus, the active contact and strong interfacial interactions required for adhesion are intrinsically in tension with the stable hydration needed for lubrication and antifouling. Achieving spatial decoupling of these competing functions within a single material, while preserving long-term structural integrity, remains a central unresolved challenge in wet biointerface design.

Janus hydrogel architectures, which conceptually mimic the functional stratification of biological tissues, have been widely explored to spatially segregate adhesion and lubrication/antifouling functions onto opposing surfaces[17,18]. Current fabrication strategies predominantly rely on unilateral post-modification, sharp layer-by-layer lamination, or spontaneous phase separation[16,19,20]. However, a fundamental engineering trade-off emerges: driving more profound functional polarization (maximizing adhesion on one side while optimizing lubrication on the other) inevitably amplifies the chemical and mechanical mismatch at the boundary. The resulting interfaces frequently suffer from localized stress concentration and progressive delamination under physiological shearing or dynamic tissue deformation[21-25]. Therefore, constructing a stable interfacial transition zone that preserves highly differentiated surface functions while resisting delamination remains a critical bottleneck for Janus hydrogels in long-term wet applications.

Inspired by the zone-stratified architecture of articular cartilage, which transitions seamlessly from a firmly anchored calcified zone to a hyper-lubricated superficial zone through a molecularly graded tidemark interface[26,27], we herein report a design principle for molecularly integrated Janus bilayer hydrogels. In our AP-HC system, the mechanically robust AP layer {[2-(acryloyloxy) ethyl]trimethylammonium chloride

(ATAC)/2-phenylethyl acrylate (PEA) copolymer} serves as the adhesive backing that anchors onto target substrates through hydrophobic and electrostatic interactions, while the highly hydrated HC layer [aldehyde-functionalized hyaluronic acid (HA-CHO)/amine-functionalized carboxymethyl cellulose ($CMC-NH_2$) polysaccharide network] functions as the biomimetic superficial layer providing lubrication and cell-repellent defense. Crucially, rather than stacking preformed layers, we employ a precursor infiltration and topological entanglement strategy: when the water-rich HC precursor is applied onto the saline-equilibrated AP substrate, it induces localized surface swelling and promotes macromolecular interdiffusion across the boundary. Subsequent *in situ* Schiff base crosslinking between HA-CHO and $CMC-NH_2$ locks these interpenetrated chains into a molecularly continuous transition zone. This integrated fabrication approach generates a Janus hydrogel that exhibits pronounced functional asymmetry in wettability, adhesion, and lubrication while maintaining stable interlayer bonding under prolonged immersion, ultrasonic disturbance, and cyclic deformation. Through this structure-defined division of functions, the AP-HC hydrogel demonstrates that spatially decoupled interfacial functions can be realized within a single integrated material, providing a conceptual framework for designing complex wet biointerface systems based on interfacial engineering principles.

EXPERIMENTAL

Materials

Carboxymethyl cellulose sodium salt (CMC, M_w = 250,000), hyaluronic acid (HA, M_w = 40-100 kDa, > 97%), sodium periodate ($NaIO_4$, analytical grade), N-(3-dimethylaminopropyl)-N'-ethylcarbodiimide hydrochloride (EDC), 1-hydroxybenzotriazole hydrate (HOBt), and phosphate-buffered saline (PBS, pH 7.4) were purchased from Macklin Biochemical Co., Ltd. (Shanghai, China). ATAC and PEA were obtained from Aladdin Biochemical Technology Co., Ltd. (Shanghai, China). Alpha-ketoglutaric acid and N,N'-methylenebisacrylamide (MBAA) were purchased from Sigma-Aldrich. Calcein-AM/PI live/dead staining kit, Cell Counting Kit-8 (CCK-8), and bicinchoninic acid (BCA) protein assay kit were purchased from Beyotime Biotechnology Co., Ltd. (Shanghai, China). Bovine serum albumin (BSA) was obtained from Beijing Solarbio Science & Technology Co., Ltd. (Beijing, China). Rabbit whole blood was supplied by Zhengzhou Ruiping Biotechnology Co., Ltd. (Zhengzhou, China). The L-929 mouse fibroblasts were purchased from Procell Life Science & Technology Co., Ltd. (Wuhan, China). Deionized water was produced using a WP-UPT-20 water system (Water Purifier ultrapure, > 18.2 $M\Omega \cdot cm^{-1}$). All reagents were used as received without further purification.

Preparation of AP-gel

AP-gels were prepared by one-step free-radical copolymerization of ATAC and PEA. The detailed formulations are summarized in Supplementary Table 1. Briefly, ATAC, PEA, α-ketoglutaric acid, and MBAA were dissolved in dimethyl sulfoxide (DMSO) and magnetically stirred at 25 °C and 450 rpm for 30 min to obtain a homogeneous precursor solution. The solution was then injected into a glass mold composed of two glass plates separated by a 0.5 mm spacer. Photopolymerization was carried out in a glovebox under 365 nm ultraviolet (UV) irradiation for 12 h. The gels were then equilibrated in physiological saline for at least 3 days, with the saline replaced every 12 h, to obtain dimensionally stable adhesive hydrogels. The resulting hydrogels were denoted as AP-gels.

Preparation of HC-gel

HA-CHO and $CMC-NH_2$ were synthesized according to previously reported procedures[28,29]. The functionalization degrees of HA-CHO and $CMC-NH_2$ were 34.8% and 27.1%, respectively [Supplementary Table 2]. To prepare HC-gels, HA-CHO and $CMC-NH_2$ were separately dissolved in deionized water by magnetic stirring at 25 °C and 450 rpm for 10 min to obtain homogeneous aqueous solutions at 1% (w/v). The HA-CHO and $CMC-NH_2$ solutions were mixed at a volume ratio of 1:1 using a vortex mixer at 1,500

rpm for 30 s at 25 °C, allowing rapid and homogeneous formation of dynamic Schiff-base crosslinks. The theoretical CHO/NH_2 molar ratio was approximately 1:1.25, as detailed in Supplementary Table 2 and the accompanying description in the Supplementary Materials. The obtained hydrogels were denoted as HC-gels.

Preparation of AP-HC bilayer hydrogel

To control the HC layer thickness, approximately 0.5 mL of freshly prepared HC precursor was uniformly blade-coated onto one side of a saline-equilibrated AP-gel with a surface area of 50 × 50 mm^2. The sample was then allowed to stand at room temperature for 15 min to complete *in situ* gelation. During this process, the water-rich HC precursor permeated into the solvent-swollen AP subsurface, promoting localized interfacial swelling and chain interdiffusion, and subsequently forming a crosslinked HC layer through Schiff base chemistry. The resulting bilayer hydrogel was stored in physiological saline before use and denoted as AP-HC-gel. According to the AP-gel formulations, the samples were named AP-HC-1, AP-HC-2, and AP-HC-3. Detailed compositions are provided in Supplementary Table 1.

Material characterization

Fourier-transform infrared spectra were recorded in attenuated total reflectance mode using a Fourier-transform infrared (FTIR) spectrometer (INVENIO-S, Bruker, Germany). The morphology and cross-sectional microstructures of the hydrogels were examined using a field-emission scanning electron microscope (FE-SEM, GEMINI SEM 360, Zeiss, Germany). Before SEM observation, hydrogel samples were cryo-fractured in liquid nitrogen, freeze-dried, and sputter-coated with gold. Optical transmittance spectra were collected using a UV-vis spectrophotometer (LAMBDA 1050, PerkinElmer, USA) over the wavelength range of 200-800 nm. Hydrogel discs with a thickness of 1 mm were used for the measurement. Surface wettability was evaluated by water contact angle measurements at room temperature using a contact angle analyzer (DSA100S; KRÜSS, Germany). For Janus bilayer samples, the AP and HC surfaces were measured separately to characterize their asymmetric wettability. Water contact angles were recorded immediately after complete droplet deposition onto the sample surface. For X-ray photoelectron spectroscopy (XPS) analysis (ESCALAB Xi+; Thermo Scientific, USA), all binding energies were charge-corrected by referencing the C–C/C–H component of the C 1s spectrum to 284.8 eV, and the corresponding energy shift was uniformly applied to all core-level spectra of each sample. The surface morphology of AP-HC was observed using an optical microscope (BDS500-FL; OPTEC, China).

Mechanical testing

Tensile tests were performed using an Instron universal testing machine equipped with a 50 N load cell (5969; Instron, USA). Hydrogel samples were cut into dumbbell-shaped specimens according to the JIS-K6251-7 standard, with an initial gauge length of 12 mm. The tests were conducted in air at a constant crosshead speed of 100 mm·min^{-1}.

For cyclic loading-unloading tensile tests, a single AP-HC-2 specimen was sequentially subjected to loading-unloading cycles at maximum strains of 100%, 200%, 300%, 400%, and 500%, with one cycle at each strain level. All cycles were performed at a crosshead speed of 100 mm·min^{-1} without resting intervals between successive cycles.

For self-recovery tests, a separate AP-HC-2 specimen was subjected to three successive loading-unloading cycles at a fixed maximum strain of 400% and a crosshead speed of 100 mm·min^{-1}. After the first cycle, the specimen was allowed to recover under unloaded conditions for 1 min before the second cycle, followed by a 2 min recovery interval before the third cycle.

For compression tests, AP-gel and HC-gel were separately prepared as cylindrical specimens with a diameter of 10 mm and a height of 4 mm. The specimens were subjected to unconfined compression using a universal

testing machine (5969; Instron, USA) at a crosshead speed of 0.5 mm·min^{-1} until 60% compressive strain was reached. The compressive modulus was calculated from the slope of the stress–strain curves within 2%-7% strain. Data are presented as mean ± standard deviation (SD) (n = 3).

Evaluation of underwater adhesion

The underwater adhesion performance of AP-gels was evaluated by lap-shear tests, 180° peeling tests, and underwater probe tack tests using a universal testing machine (CMT-1503, SANS, China). Before testing, all substrates were rinsed sequentially with ethanol and deionized water. For lap-shear tests, a hydrogel sample with dimensions of 20 × 20 × 1 mm^3 was placed between two substrates and compressed at 10 kPa for 30 s to form an adhesive joint. The bonded samples were then stretched at a crosshead speed of 5 mm·min^{-1}. The lap-shear adhesion strength was calculated by dividing the maximum force by the bonded area. To evaluate long-term underwater adhesion stability, the bonded joints were immersed in water at 37 °C for predetermined periods before testing. For 180° peeling tests, hydrogel specimens (20 × 20 × 1 mm^3) were adhered to polyethylene terephthalate (PET) substrates under 10 kPa for 30 s. The peeling test was performed at a rate of 5 mm·min^{-1}. The interfacial toughness was calculated according to:

$$\text{Interfacial toughness} = \left(\frac{2F_{plateau}}{w}\right)$$

Where $F_{plateau}$ is the plateau tension, and w is the width of the adhesion surface[30].

For underwater probe tack tests, circular hydrogel samples with a diameter of 10 mm and a thickness of 1 mm were fixed onto the probe using cyanoacrylate adhesive. The probe with the attached hydrogel was immersed in the testing solution for 5 min before measurement. During testing, the probe approached the substrate at 10 mm·min^{-1}, remained in contact for 30 s under a preset load, and was then withdrawn at 10 mm·min^{-1}. The adhesion strength and work of adhesion were calculated from the force-displacement curves.

Lubrication performance evaluation

The lubrication performance of hydrogel surfaces was evaluated using the tribology mode of a TA rheometer (ARES-G2; TA Instruments, USA) equipped with a three-ball fixture. Circular hydrogel samples, with a thickness of 2 mm and a diameter of 40 mm, were fixed on the lower plate as the friction substrate. To assess the robustness of lubrication, friction measurements were further conducted under different normal loads, sliding frequencies, immersion durations, and media conditions. For physiologically relevant tests, PBS, serum, and PBS containing BSA were used as lubricating media at 37 °C. The coefficient of friction (COF) was recorded as a function of sliding time. Unless otherwise specified, friction tests were conducted under a normal load of 0.25 N at a sliding frequency of 1 Hz. All measurements were performed under the specified lubricating conditions, and the COF was continuously recorded throughout the test. Each condition was tested using at least n = 3 independent hydrogel samples.

Antibiofouling test

Anti-cell-adhesion assay

The cell-repellent behavior of the hydrogel surfaces was evaluated using L929 mouse fibroblasts. Before cell seeding, hydrogel samples were sterilized and placed in culture plates. Fluorescently labeled L929 cells were seeded onto the sample surfaces at a density of 1 × 10^5 cells per sample and incubated at 37 °C in a humidified atmosphere containing 5% CO_2 for 24 h. After incubation, the samples were gently rinsed with PBS to remove non-adherent cells. The remaining adherent cells were observed by fluorescence microscopy (Axio observer3, Carl Zeiss Microscopy GmbH, Germany). The number of attached cells was quantified from fluorescence images to evaluate the anti-cell-adhesion performance of the HC surface.

Anti-protein-adhesion assay

The protein adsorption assay was performed according to a previously reported method[14], using BSA as the model protein. The samples were immersed in a BSA solution with a concentration of 0.5 mg/mL and incubated at 37 °C for 2 h. After incubation, the samples were thoroughly rinsed with PBS to remove loosely bound proteins. Subsequently, the samples were immersed in a 2 wt% sodium dodecyl sulfate (SDS) solution and ultrasonicated for 30 min to fully desorb the adsorbed proteins. Finally, the protein content was determined at 562 nm using a microplate reader according to the instructions of the BCA protein assay kit, and the amount of protein adsorbed on the sample surface was calculated (INFINITE 200 PRO, Tecan Austria GmbH, Austria). The amount of adsorbed BSA was determined from the BSA concentration in the desorption solution and normalized to the exposed surface area of the hydrogel.

Stability of the HC functional layer

The interfacial stability of the HC layer on the AP substrate was evaluated by ultrasonic treatment, long-term immersion, and cyclic mechanical deformation. For ultrasonic stability tests, AP-HC samples were immersed in water and ultrasonicated (40 kHz) for 30 or 60 min. After treatment, the water contact angle of the HC surface was measured to assess the retention of surface hydration. For long-term aqueous stability tests, AP-HC samples were immersed in deionized water for predetermined durations. The water contact angle of the HC surface was monitored over time. Cross-sectional morphology after immersion was further examined to determine whether interfacial delamination occurred. For mechanical stability tests, AP-HC samples were cut into rectangular strips with dimensions of 5 cm × 1 cm and subjected to 1,000 stretching cycles at a strain of 200% using a fatigue tester at a rate of 50 mm·min^{-1} (EDT102A; Kewotest, China). After cycling, the water contact angles of both AP and HC surfaces were measured to evaluate whether the Janus wettability contrast was retained.

Hemolysis assay

The hemocompatibility of AP-HC hydrogels was assessed by a hemolysis assay using a 2% erythrocyte suspension in saline. Hydrogel samples were incubated with the erythrocyte suspension at 37 °C for 1 h. After incubation, the suspensions were centrifuged at 1,000 rpm for 10 min, and the absorbance of the supernatant was measured at 542 nm using a UV-vis spectrophotometer (LAMBDA 1050, PerkinElmer, USA).

$$Hemolysis\ (\%) = \frac{(OD_h - OD_n)}{(OD_p - OD_n)} \times 100\%$$

where OD_h, OD_n, and OD_p represent the absorbance values of the hydrogel, negative control, and positive control, respectively[31].

Cytocompatibility evaluation

The cytocompatibility of AP-HC was evaluated using the extract method. Wet, fully formed AP-HC hydrogel was immersed in complete culture medium at a ratio of 0.2 g·mL^{-1} and incubated at 37 °C for 24 h. The resulting extract was then applied to the cells for 24 h, after which cell viability was evaluated using the CCK-8 assay. Briefly, CCK-8 solution was added to each well and incubated according to the manufacturer's protocol. The optical density at 450 nm was measured using a microplate reader (INFINITE 200 PRO, Tecan Austria GmbH, Austria). In addition, cell viability was visualized by live/dead staining using a Calcein/PI Cell Viability/Cytotoxicity Assay Kit, followed by fluorescence microscopy observation (Axio observer3, Carl Zeiss Microscopy GmbH, Germany).

Statistical analysis

All data are presented as mean ± SD from at least three independent experiments. Statistical analyses were conducted using GraphPad Prism software. Comparisons between two groups were evaluated using an

unpaired two-tailed Student's *t*-test, while comparisons among multiple groups were performed using one-way analysis of variance (ANOVA) followed by Tukey's multiple-comparisons post-hoc test. Significance levels were denoted as ns (not significant), $^{*}P < 0.05$, $^{**}P < 0.01$, $^{***}P < 0.001$, and $^{****}P < 0.0001$.

RESULTS AND DISCUSSION

Design principle and structural characterization of the Janus bilayer hydrogel

Natural protective soft tissues, such as articular cartilage, skin, and fish scales, adopt a zone-stratified design in which a highly hydrated, bioinert surface provides lubrication or biofouling resistance while the opposing side merges into a mechanically robust matrix for structural support[32]. This biological paradigm suggests that functionally opposed interfacial properties can coexist within a single material if they are spatially organized across a structurally continuous interface. Inspired by this principle, we designed an asymmetric AP-HC bilayer hydrogel to decouple wet adhesion and hydrated lubrication across two opposing surfaces [Figure 1A and B]. In this configuration, the AP layer provides adhesion and mechanical support, while the HC layer serves as the hydrophilic, lubricating, and cell-repellent surface.

The AP-HC hydrogel was fabricated through a sequential interfacial construction strategy [Figure 1A]. The fabrication process is schematically illustrated in Supplementary Figure 1. The AP layer was first prepared by photopolymerization of ATAC and PEA, followed by saline equilibration to achieve dimensional stability. An aqueous HC precursor containing HA-CHO and CMC-NH_2 was then coated onto one side of the AP gel and gelled *in situ* through Schiff base reaction. Rheological analysis showed that the crossover of G' and G'' confirmed the rapid gelation and network formation of HC-gel after mixing HA-CHO and CMC-NH_2 solutions [Supplementary Figure 2]. Critically, this process differs from simple layer-by-layer deposition in a mechanistically important way: the water-rich HC precursor permeates into the solvent-swollen AP subsurface, allowing partial diffusion of HA-CHO and CMC-NH_2 chains into the near-surface AP network. The subsequent Schiff base crosslinking locks these interdiffused chains in place, generating an interpenetrating network-like transition region. The resulting bilayer is thus integrated through precursor infiltration, molecular interdiffusion, and *in situ* crosslinking, which is expected to enhance structural stability and resist delamination under wet and dynamic conditions[27,28]. After optimization, AP-2 and AP-HC-2 were selected as the representative formulations for AP gel and AP-HC Janus hydrogel, respectively, and were used for subsequent experiments unless otherwise specified.

The construction of the bilayer structure was first investigated by using cross-sectional SEM, where a continuous interface between the AP and HC layers was observed without obvious cracking or separation [Figure 1C]. Cross-sectional optical microscopy revealed HC and AP layer thicknesses of approximately 76 and 570 μm, respectively, in the AP-HC bilayer hydrogel [Supplementary Figure 3]. The two sides showed sharply different surface wettability: the AP side exhibited a relatively high water contact angle of approximately 93.5°, whereas the HC side showed a very low value of approximately 19.7° [Figure 1D]. This strong wettability contrast confirms the Janus character of the AP-HC hydrogel. Consistently, the AP side demonstrated obvious adhesion to the substrate, while the HC side displayed negligible adhesion [Figure 1E], directly showing that wet adhesion and anti-adhesion are effectively separated onto opposite surfaces of one integrated hydrogel.

The functional asymmetry was further supported by cell-adhesion and mechanical measurements. Hydrogel samples were placed in 48-well plates and fluorescently labeled L929 cell suspensions were seeded onto the hydrogel surfaces. After 24 h of incubation followed by PBS washing, only a small number of L929 cells remained adhered to the HC surface [Figure 1F], indicating that the hydrated layer on the HC surface effectively suppressed cell adhesion. Meanwhile, compression tests of the separately prepared AP-gel and HC-gel showed that AP-gel exhibited a substantially higher compressive modulus than HC-gel [Figure 1G

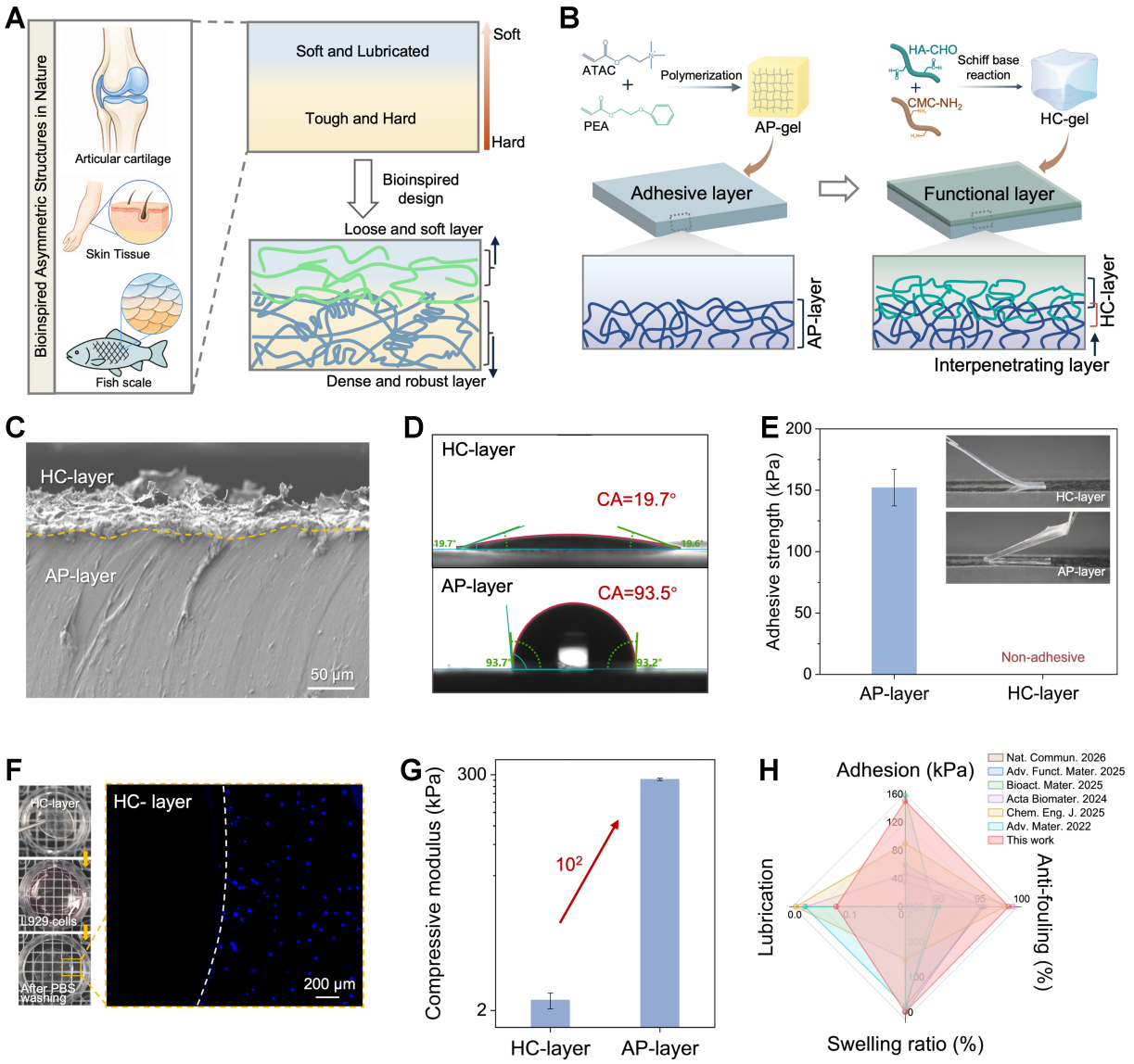


Figure 1. Design and structural characterization of the AP-HC bilayer hydrogel. (A) Schematic illustration of asymmetric biological architectures, including articular cartilage, skin tissue, and fish scales, inspiring the Janus bilayer design; (B) Formation of the HC hydrogel layer on the AP substrate through *in situ* Schiff base crosslinking between HA-CHO and CMC-NH_2, accompanied by interfacial chain interdiffusion and network interpenetration; (C) Cross-sectional SEM image of the AP-HC bilayer hydrogel; (D) Water contact angles of the adhesive AP side and the hydrated lubricating HC side; (E) Comparison of the asymmetric adhesion behavior of the two surfaces of the intact AP-HC hydrogel, showing adhesion on the AP side and negligible adhesion on the HC side; (F) Representative fluorescence images showing reduced L929 cell attachment on the HC surface after 24 h culture and PBS washing; (G) Comparison of the compressive moduli of separately prepared AP-gel and HC-gel; (H) Radar plot comparing the integrated performance of AP-HC with previously reported hydrogel systems[18,33-37]. Data are presented as mean ± SD (n = 3 independent samples). HA-CHO: Aldehyde-functionalized hyaluronic acid; CMC-NH_2: amine-functionalized carboxymethyl cellulose; SEM: scanning electron microscope; PBS: phosphate-buffered saline; SD: standard deviation; ATAC: [2-(acryloyloxy) ethyl]trimethylammonium chloride; PEA: 2-phenylethyl acrylate.

and Supplementary Figure 4], supporting the mechanical contrast between the relatively stiff AP supporting layer and the soft hydrated HC layer in the bilayer architecture. Finally, a radar comparison indicates that AP-HC achieves a balanced combination of wet adhesion, anti-swelling stability, antibiofouling behavior, and lubrication compared with reported hydrogel systems [Figure 1H]. Together, these results establish AP-HC as an integrated Janus hydrogel platform in which spatially decoupled functions are realized through a structure-defined design rather than through simple compositional layering.

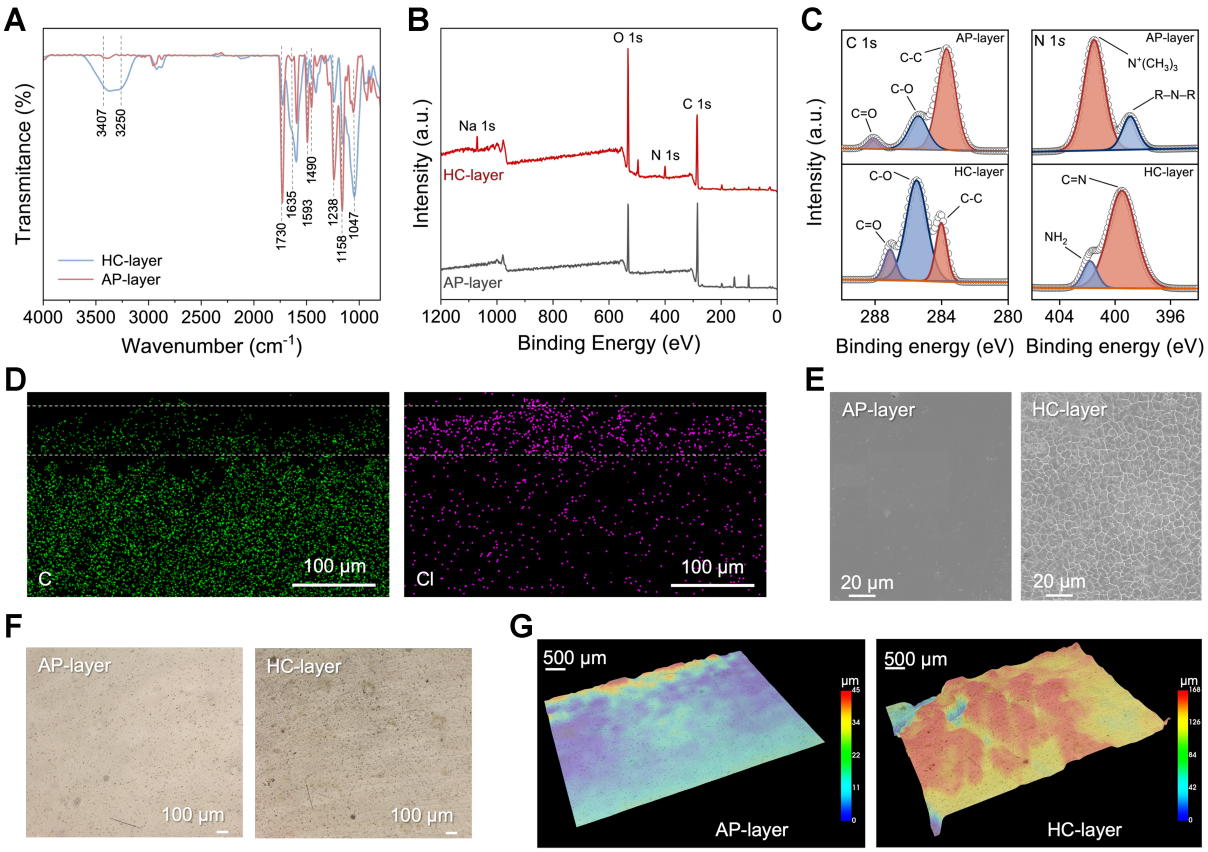


Figure 2. Interfacial chemical and structural asymmetry of the AP-HC bilayer hydrogel. (A) ATR-FTIR spectra of the AP-layer and HC-layer surfaces of AP-HC; (B) XPS survey spectra of the AP-layer and HC-layer surfaces of AP-HC; (C) High-resolution XPS C 1s and N 1s spectra collected from the AP-layer and HC-layer regions of AP-HC; (D) Cross-sectional EDS elemental mappings of C and Cl in the AP-HC gel; (E) SEM images of the cross-sectional microstructures in the AP-layer and HC-layer regions of AP-HC; (F) Optical microscopy images of the AP-layer and HC-layer sides of the bilayer hydrogel; (G) Three-dimensional surface profilometry maps of the AP-layer and HC-layer surfaces of AP-HC. ATR-FTIR: Attenuated total reflectance Fourier-transform infrared; XPS: X-ray photoelectron spectroscopy; EDS: energy-dispersive X-ray spectroscopy; SEM: scanning electron microscope.

Interfacial chemical and structural asymmetry of the AP-HC bilayer hydrogel

To verify that the observed Janus functions arise from genuine chemical and structural asymmetry rather than from surface-limited effects, we characterized the composition, cross-sectional element mapping, and surface topology of AP-HC using complementary techniques. Attenuated total reflectance Fourier-transform infrared (ATR-FTIR) spectra revealed distinct molecular signatures on the two surfaces [Figure 2A]. The HC side showed typical polysaccharide-derived absorption bands, including a broad O–H/N–H stretching band at 3,200-3,500 cm^{-1} and strong C–O–C/C–O stretching vibrations at 1,000-1,150 cm^{-1}. The absorption around 1,600-1,650 cm^{-1} can be assigned to imine (C=N) bonds, with possible overlap from carbonyl/carboxylate-related vibrations, supporting the Schiff base reaction between HA-CHO and CMC-NH_2. The AP side exhibited characteristic peaks of an acrylate-based copolymer network, including ester C=O stretching at 1,720-1,730 cm^{-1} and C–O stretching vibrations in the 1,150-1,250 cm^{-1} region. In addition, the distinct absorption bands at 1,593 and 1,490 cm^{-1}, corresponding to the skeletal vibrations of aromatic rings, further indicate the presence of PEA segments on the AP side[38,39]. These results confirm that the AP-layer and HC-layer are chemically distinct.

XPS further supported the surface chemical asymmetry [Figure 2B and C]. The survey spectra showed clear differences in the N 1s signals between the two sides. On the AP side, the nitrogen signal mainly originated from quaternary ammonium groups in ATAC, whereas the HC side contained imine nitrogen associated

with Schiff base formation, together with residual Na^+ from the polysaccharide components. High-resolution C 1s spectra showed peaks at 284.8, 286.0, and 288.5 eV on the AP side, corresponding to hydrocarbon species, C–O/ester-related carbon species, and carbonyl/ester-related carbon species, respectively. By comparison, the HC side was dominated by C–O/C–O–C species at approximately 286.4 eV and carbonyl-related peaks. The N 1s spectrum of the HC side displayed a distinct C=N peak at 399.8 eV, further confirming the dynamic covalent crosslinked HC network. Together, ATR-FTIR and XPS results demonstrate that AP-HC is a compositionally asymmetric bilayer system, composed of a cationic acrylate AP layer and a polysaccharide-rich HC layer.

The structural basis of this asymmetry was visualized by cross-sectional SEM with elemental mapping [Figure 2D and E]. Additional SEM images of the adhesive side, lubricating side, and full cross-section of the bilayer are provided in Supplementary Figure 5. The HC region exhibited a more porous network morphology, consistent with a hydrated polysaccharide hydrogel [Supplementary Figure 6], whereas the AP region appeared substantially denser, which is a structural feature favorable for mechanical support and swelling resistance. Despite the pronounced difference in swelling behavior between the two layers, the compliant HC layer can accommodate local deformation, while constrained swelling on curved substrates may generate a gradient deformation profile that helps alleviate interfacial stress concentration [Supplementary Figure 7]. This buffering effect may help maintain the long-term structural stability of the AP-HC interface. Elemental mapping confirmed the compositional difference across the thickness direction. Importantly, no obvious crack or sharp delamination boundary was observed at the interface, indicating that the two layers are tightly integrated rather than physically stacked. The interfacial bonding strength was further evaluated by lap-shear tests [Supplementary Figure 8]. Compared with the preformed AP/HC contact interface, the *in situ* polymerized AP-HC interface exhibited cohesive failure within the hydrogel, indicating that precursor infiltration followed by *in situ* gelation effectively strengthens the interfacial bonding. To qualitatively verify precursor infiltration, HA-CHO was applied onto the AP surface and visualized by Schiff reagent staining[40]. The stained optical images revealed that HA-CHO penetrated into the superficial region of the AP network [Supplementary Figure 9], providing qualitative evidence for localized infiltration of the polysaccharide-based HC precursor. This continuous interface supports the proposed mechanism of precursor infiltration, molecular interdiffusion, and *in situ* crosslinking. In addition, optical microscopy and three-dimensional profilometry revealed distinct surface topographies on the two sides [Figure 2F and G]: the AP side was relatively smooth, while the HC side showed more pronounced surface fluctuations, reflecting the intrinsic structural difference between the compact adhesive network and the hydrated polysaccharide layer. This asymmetric microstructure provides the physical basis for the differential wet adhesion, lubrication, and antibiofouling behaviors characterized in the following sections.

Mechanical performance and water stability of the AP-HC bilayer hydrogel

For bilayer systems intended for wet biomedical applications, uncontrolled water uptake can cause swelling mismatch between layers, generating interfacial stress and eventual delamination. Therefore, we systematically evaluated the mechanical robustness, water stability, and structural integrity of AP-HC. AP-HC exhibited good macroscopic integrity and retained its original shape after 24 h of water immersion, indicating excellent anti-swelling stability [Figure 3A and B]. Quantitative analysis showed that AP-HC maintained a high water content while displaying a limited swelling ratio [Figure 3C]. This combination is important because sufficient water retention is necessary for softness, lubrication, and biological compatibility, whereas excessive swelling would weaken the network and compromise the bilayer interface. The anti-swelling behavior can be attributed to the AP supporting layer, in which hydrophobic PEA segments, ionic interactions from ATAC, and saline equilibration collectively restrict uncontrolled network expansion. The stable appearance after water immersion further confirms that the AP and HC layers are well integrated, with no macroscopic delamination caused by swelling mismatch.

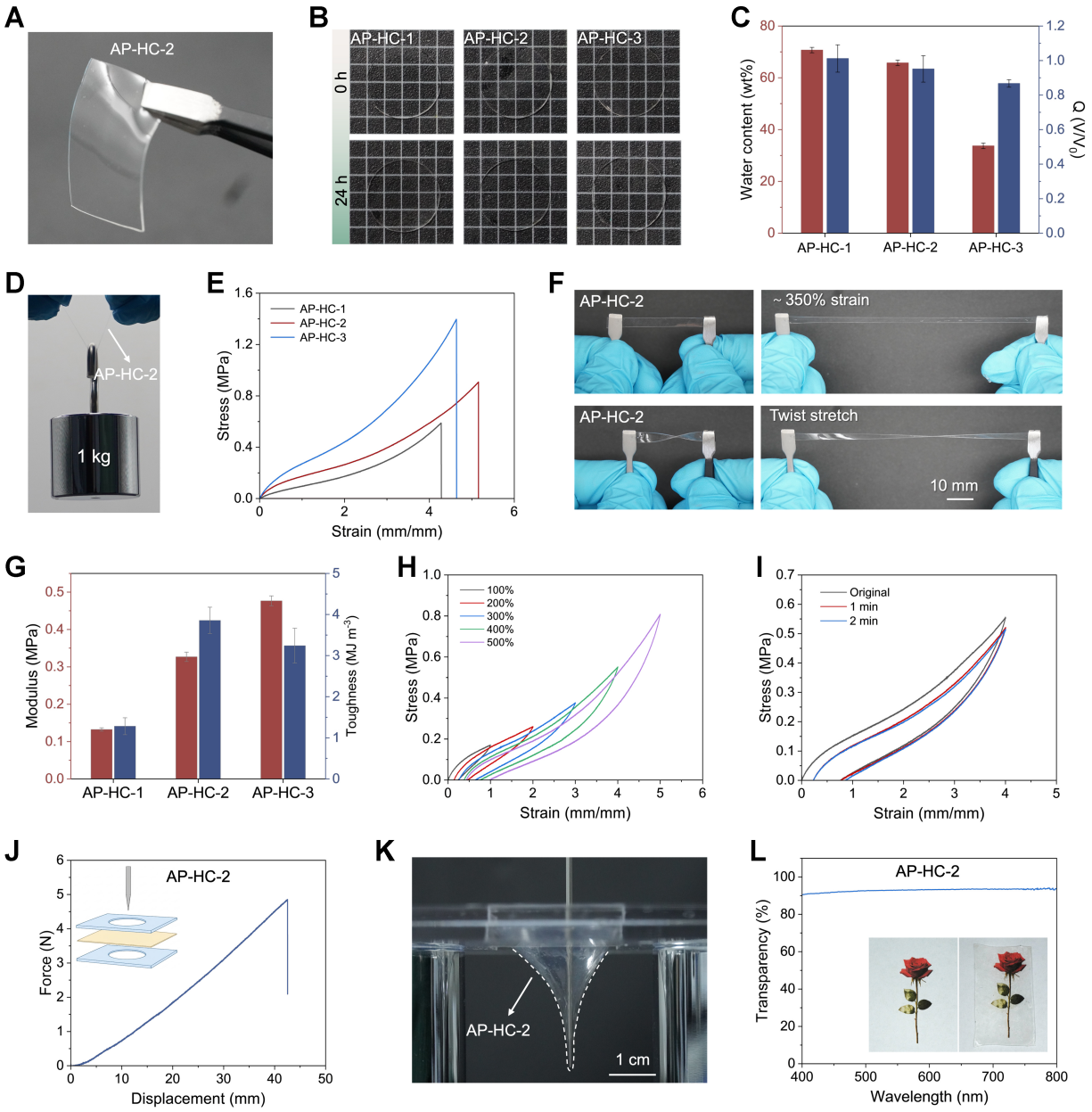


Figure 3. Mechanical performance and water stability of the AP-HC bilayer hydrogel. (A) Photograph of AP-HC; (B) Photographs of AP-HC after immersion in water for 0 and 24 h, showing anti-swelling capability and structural integrity; (C) Water content and swelling ratio of the AP-HC hydrogels ($Q = V_t/V_0$ is defined as the volumetric swelling ratio, where V_0 and V_t represent the initial hydrogel volume and the volume after immersion, respectively. A value of $Q > 1$ indicates swelling, whereas $Q < 1$ indicates volume shrinkage); (D) Photograph showing that AP-HC can lift a 1 kg weight; (E) Tensile stress-strain curves of hydrogels with different compositions; (F) Photograph demonstrating the high stretchability of AP-HC; (G) Young's modulus and toughness of the hydrogels; (H) Cyclic loading–unloading curves of AP-HC-2 at increasing strains (100%-500%) without resting intervals; (I) Self-recovery curves of AP-HC-2 at 400% strain with 1 and 2 min recovery intervals; (J and K) Puncture resistance profiles and demonstration of structural integrity against sharp objects; (L) UV-vis transmittance spectra and optical transparency of AP-HC. Data are presented as mean ± SD (n = 3 independent samples). UV: Ultraviolet; SD: standard deviation.

The mechanical integrity of AP-HC was then examined under tensile and load-bearing conditions. The hydrogel lifted a 1 kg weight without failure [Figure 3D], directly demonstrating its high structural strength. Tensile stress-strain curves showed high stretchability and considerable fracture resistance, and AP-HC could be elongated substantially while maintaining continuity [Figure 3E and F]. The calculated Young's modulus (0.33 MPa) and toughness (3.86 MJ·m^{-3}) confirmed a favorable balance between stiffness and energy

dissipation [Figure 3G]. Frequency-dependent viscoelastic behavior, characterized by storage and loss moduli, is presented in Supplementary Figure 10. This balanced mechanical response is essential for biointerface applications, where the material must be compliant enough to match soft tissues but strong enough to resist deformation and tearing.

To further assess its mechanical stability, AP-HC was subjected to cyclic loading–unloading tests under repeated deformation. Under stepwise increasing strain, obvious hysteresis loops were observed [Figure 3H], indicating effective internal energy dissipation during deformation. The hysteresis and self-recovery behavior [Figure 3I] suggest that part of the dissipated network structure can recover after unloading, which benefits fatigue resistance under repeated mechanical stimulation. In addition, AP-HC showed strong puncture resistance and maintained structural integrity against sharp objects [Figure 3J and K], confirming that the material behaves as a tough integrated hydrogel rather than a weakly attached coating. Under humid physiological-like conditions (~37 °C), the hydrogel exhibited mechanical responses comparable to those measured in air at room temperature, indicating stable mechanical performance under humid conditions [Supplementary Figure 11]. Meanwhile, AP-HC retained good optical transparency [Figure 3L], which may be useful for tissue-contacting biointerfaces requiring optical access, such as endoscopic imaging systems and fiber-optic OCT catheters/endoscopes that rely on clear optical windows to visualize internal tissues during minimally invasive diagnosis or intervention[41,42]. Overall, these results demonstrate that AP-HC combines water stability, toughness, recoverable energy dissipation, puncture resistance, and transparency, providing a reliable mechanical foundation for its subsequent adhesive, lubricating, and antibiofouling functions.

Wet adhesion of the AP layer

With the mechanical robustness of the bilayer confirmed, we focused on the primary function of the adhesive AP layer. Wet adhesion was evaluated using three complementary test configurations including lap-shear, 180° peeling, and probe tack, to capture the distinct loading modes (shear, peel, and tensile pull-off) encountered at practical biointerfaces [Figure 4A-I]. In the lap-shear configuration on polyvinyl chloride (PVC) substrates, AP-gel exhibited clear force buildup and high shear adhesion strength, indicating strong resistance to interfacial sliding underwater [Figure 4B and C]. The 180° peel test on PET films showed stable peeling resistance and considerable interfacial toughness, suggesting effective energy dissipation during crack propagation along the interface [Figure 4D-F]. Underwater probe tack tests on negatively charged glass further revealed pronounced pull-off forces and high adhesion work, confirming rapid and robust contact formation in a hydrated environment [Figure 4G-I]. Visual demonstrations further supported this strong adhesion: a small AP-gel sample could connect two PVC plates and suspend a heavy load, and it could also adhere to a 1.0 kg weight underwater and lift it out of water without detachment [Figure 4J and K]. These results demonstrate that AP-gel maintains reliable wet adhesion across sliding, peeling, and tensile pull-off loading conditions. Considering the asymmetric functional design of the AP-HC Janus hydrogel, the adhesion performance of the intact bilayer structure was further evaluated by probe tack testing [Supplementary Figure 12]. The comparable adhesion strengths of AP-gel and AP-HC confirm that incorporation of the HC layer does not compromise the adhesive performance of the AP layer.

The wet adhesion performance can be rationalized through the cooperative molecular design of the AP network. The hydrophobic PEA segments likely help disrupt interfacial hydration layers and promote direct polymer-substrate contact, while the cationic ATAC units provide electrostatic attraction toward polar or weakly charged substrates, such as glass and PVC[10,43-45]. Beyond interfacial interactions, the covalently crosslinked AP network offers sufficient cohesion to prevent cohesive failure during loading, and reversible physical interactions within the network contribute to energy dissipation that slows interfacial crack growth. Together, the combination of interfacial adhesion and bulk energy dissipation enables AP-gel to maintain stable attachment under diverse mechanical stresses and aqueous conditions.

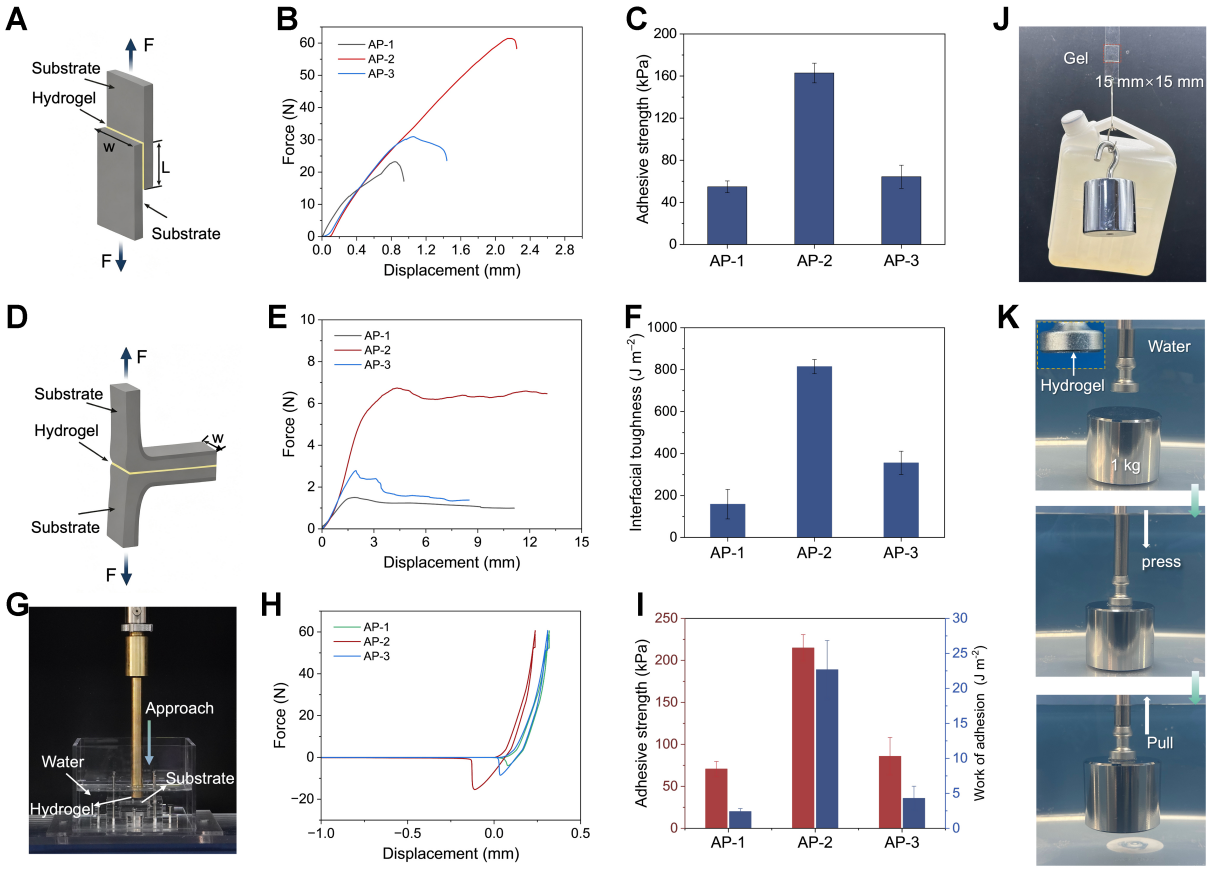


Figure 4. Underwater adhesion performance of the AP-gel. (A) Schematic illustration of the lap-shear adhesion test; (B and C) Force-displacement curves and corresponding adhesion strengths of AP-gel on PVC substrates measured by lap-shear tests. (specimen size: 20 × 20 × 1 mm^3; testing speed: 5 $mm \cdot min^{-1}$); (D) Schematic illustration of the 180° peel test; (E and F) Force-displacement curves and corresponding interfacial toughness values of AP-gel on PET film substrates measured by 180° peel tests. (specimen size: 20 × 20 × 1 mm^3; peeling speed: 5 $mm \cdot min^{-1}$); (G) Schematic illustration of the probe tack test for underwater adhesion; (H and I) Force-displacement curves, adhesion strengths, and work of adhesion of AP-gel on negatively charged glass substrates in water (specimen diameter: 10 mm; thickness: 1 mm; approach and withdrawal speeds: 10 $mm \cdot min^{-1}$); (J) Load-bearing test of a 15 by 15 mm AP-gel sample connecting two PVC plates and suspending a heavy weight; (K) Photograph showing that AP-gel can adhere to a 1.0 kg weight underwater and lift it from water into air. PVC: Polyvinyl chloride; PET: polyethylene terephthalate.

Adhesion durability and substrate versatility

Practical biointerface applications demand not only high initial adhesion but also durability and versatility. We therefore evaluated the reusability, long-term stability, and substrate scope of AP-gel adhesion. Repeated lap-shear adhesion–detachment–readhesion tests on PVC substrates showed that the AP-2 retained approximately 82.9% of its initial adhesion strength after 50 cycles, indicating good reusability despite a moderate decrease in adhesion performance [Figure 5A]. This repeatability indicates that the adhesive interface can be repeatedly reconstructed after failure, distinguishing AP-gel from single-use adhesive systems and suggesting utility in repositionable biomedical devices.

Long-term underwater adhesion stability was examined by immersing AP-2/PVC adhesive joints in water for extended durations before lap-shear testing [Figure 5B and C]. Both the force-displacement curves and the calculated adhesion strengths remained stable, with no significant decay over time. This durability is consistent with the swelling-resistant character of the AP network discussed above: by limiting excessive water uptake, the network preserves both bulk cohesion and interfacial contact, preventing progressive weakening of the adhesive joint. The dimensional stability of AP-gel thus provides the structural foundation for persistent adhesion in aqueous environments.

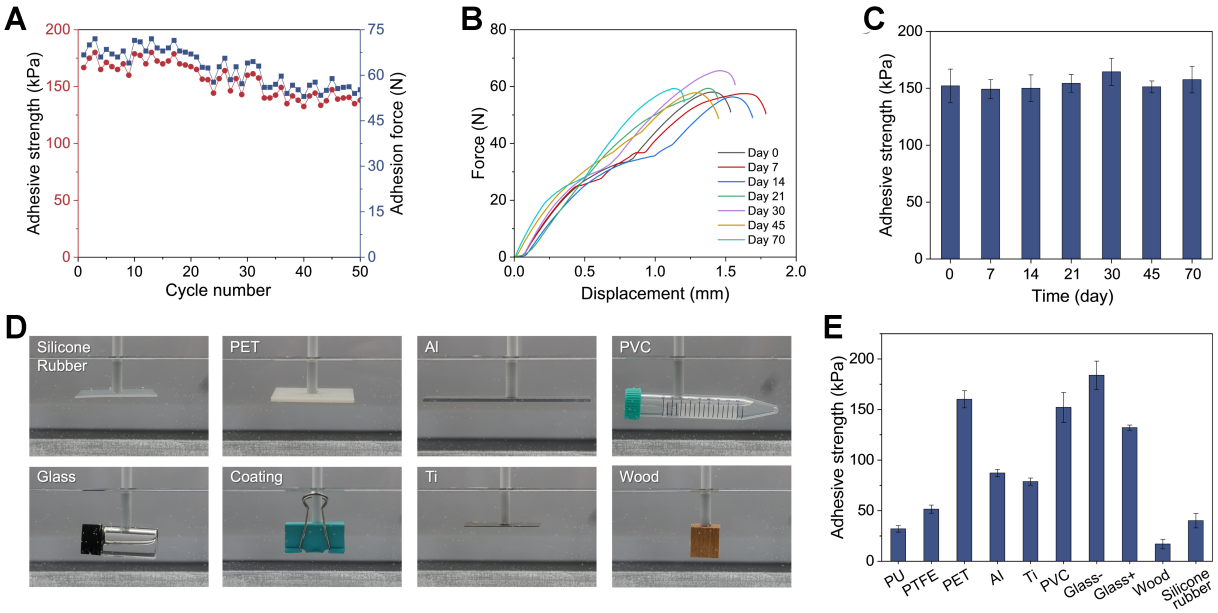


Figure 5. Underwater adhesion performance of the AP-2: durability and substrate versatility. (A) Repeatable underwater lap-shear adhesion performance of AP-2 on PVC substrates (Red circles indicate adhesive-strength data points, while blue squares indicate adhesion-force data points); (B) Force-displacement curves obtained from long-term underwater lap-shear tests of AP-2 on PVC substrates after immersion for different durations; (C) Long-term underwater lap-shear adhesion strength of AP-2 on PVC substrates after immersion in water for different periods; (D) Underwater adhesion of AP-2 to different substrates; (E) Underwater lap-shear adhesion strengths of AP-2 on various substrates. Hydrogel specimens (20 × 20 × 1 mm^3) were compressed at 10 kPa for 30 s and stretched at 5 $mm \cdot min^{-1}$. Lap-shear strength was calculated as the maximum load divided by the bonded area. Data are presented as mean ± SD (n = 3 independent samples). PVC: Polyvinyl chloride; SD: standard deviation; PET: polyethylene terephthalate; PU: polyurethane; PTFE: polytetrafluoroethylene.

The substrate versatility of AP-2 was assessed across a range of representative materials, including polymeric, metallic, inorganic, and natural substrates [Figure 5D and E]. Although the adhesion strength varied with substrate polarity, surface energy, and interfacial chemistry, as expected for a system relying on noncovalent interfacial interactions, AP-gel maintained appreciable underwater adhesion on all tested surfaces. This broad substrate tolerance can be attributed to synergistic interfacial dehydration and multiple noncovalent interactions. During brief compression, the soft and conformable AP network adapts to the substrate surface, promotes the removal of loosely bound interfacial water, and increases the effective contact area. Hydrophobic segments in the AP network reduce interfacial hydration, while van der Waals and hydrophobic interactions facilitate adhesion to low-surface-energy substrates such as PTFE and silicone rubber. These combined effects enable AP-gel to form strong adhesive bond with a wide range of substrates.

Interfacial stability and hydrated lubrication of the HC functional layer

Having established the adhesion performance of the AP layer, we next turned to the complementary function of the opposing HC surface. Two questions are critical: first, whether the HC layer remains stably attached to the AP substrate under mechanical and aqueous challenges; and second, whether the hydrated HC surface delivers effective lubrication. The AP-HC hydrogel was designed with an *in situ* interfacial growth strategy specifically to address the delamination problem common to sequentially constructed bilayer hydrogels. As shown schematically in Figure 6A, the HC network is anchored to the AP substrate through interfacial chain interdiffusion and crosslinking, generating an interpenetrated transition zone rather than a sharp boundary.

The stability of the HC layer was evaluated under multiple harsh conditions, using surface wettability as an indicator of functional-layer retention. After ultrasonic treatment for 30 and 60 min, the HC surface still maintained a low water contact angle, indicating that the hydrophilic layer was not removed by

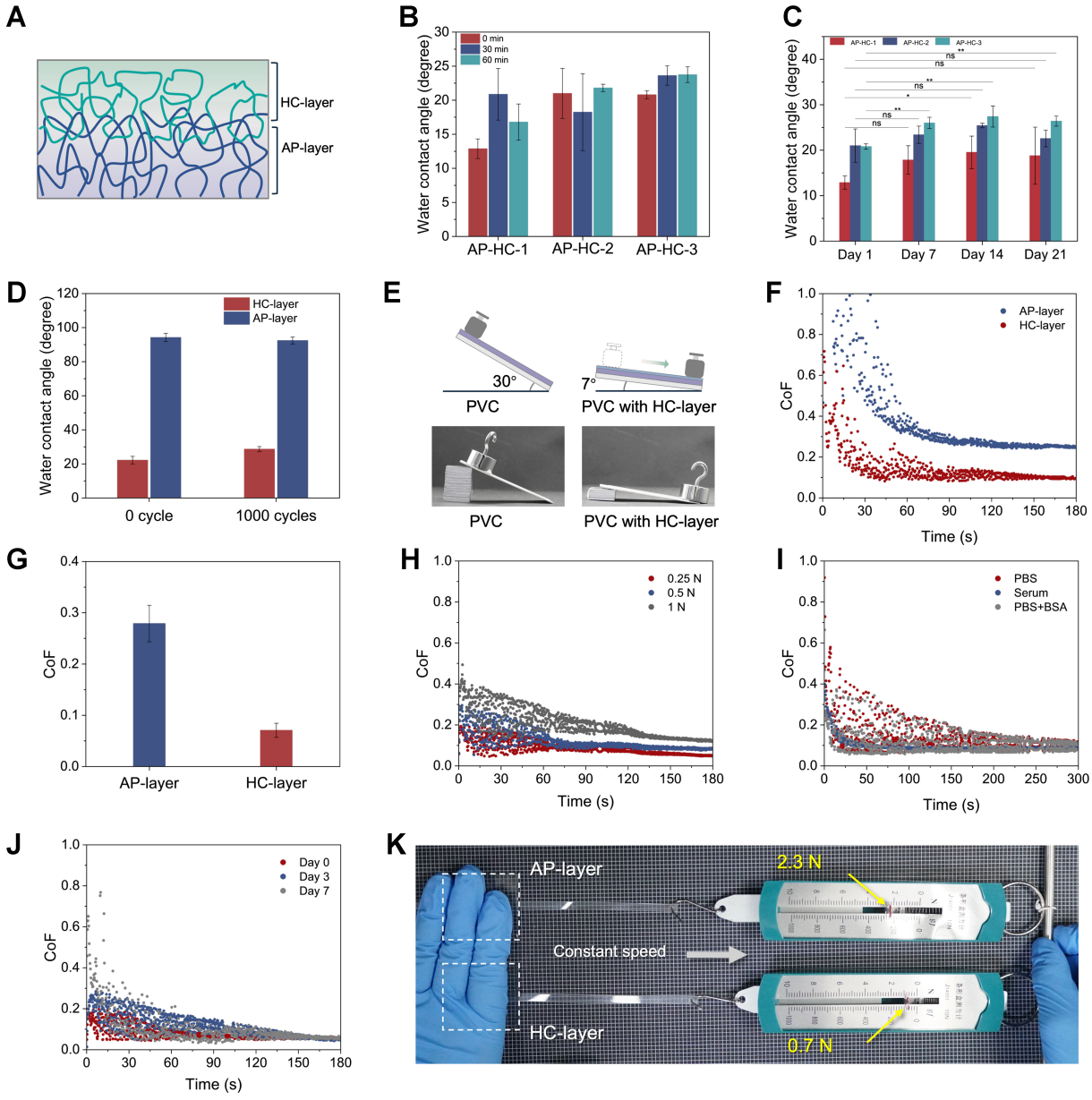


Figure 6. Interfacial stability and hydrated lubrication of the AP-HC bilayer hydrogel. (A) Schematic illustration of the interfacial integration mechanism between the adhesive layer and the hydrophilic lubricating layer in AP-HC; (B) Water contact angles of the hydrophilic lubricating layer after ultrasonic treatment for 0, 30, and 60 min; (C) Evolution of the water contact angle of the hydrophilic lubricating layer during immersion in deionized water for 21 days; (D) Water contact angles of the upper and lower surfaces of AP-HC-2 before and after 1,000 stretching cycles at a strain of 200%; (E) Schematic illustration of the friction test for bare PVC and PVC coated with AP-HC-2; (F and G) Time-dependent COF curves and corresponding average COF values of the AP layer and HC layer of AP-HC-2; (H) Lubrication performance curves of the AP-HC-2 surface measured under different normal loads; (I) Lubrication performance curves of the AP-HC-2 surface measured in different media at 37 °C, including PBS, serum, and PBS containing BSA; (J) Lubrication performance curves of the AP-HC-2 surface after immersion in water for 0, 3, and 7 days; (K) Demonstration of the low-friction behavior of the hydrophilic surface of AP-HC (a PVC strip was clamped between the functional sides or the adhesive sides of two AP-HC pieces and then pulled in the same direction using a spring dynamometer; the functional side exhibited lower friction, indicating better lubricating performance). Data are presented as mean ± SD (n = 3 independent samples). $^{**}P < 0.01$, $^{*}P < 0.05$; ns, not significant. PVC: Polyvinyl chloride; COF: coefficient of friction; PBS: phosphate-buffered saline; BSA: bovine serum albumin; SD: standard deviation.

cavitation-induced mechanical erosion [Figure 6B]. During continuous immersion in deionized water for 21 days, the water contact angle of the HC side increased modestly but remained within the hydrophilic range, indicating that the polysaccharide-rich lubricating layer did not undergo obvious dissolution or structural

reorganization [Figure 6C]. Furthermore, after 1,000 stretching cycles, the two surfaces of AP-HC-2 retained their distinct wettability characteristics [Figure 6D and Supplementary Figure 13], indicating that the asymmetric surface functions of the AP and HC layers were preserved under repeated deformation. The sustained hydrophilicity of the HC surface suggests that its hydrated interfacial function was not substantially compromised, supporting the durability of the Janus hydrogel during repeated mechanical loading.

The stable HC layer then enabled sustained hydration lubrication. The lubricating effect was first visualized by an inclined-plane demonstration [Figure 6E and Supplementary Movie 1]: a weight that did not slide on bare PVC even at a tilt angle of 30° readily slid on AP-HC-coated PVC at only 7°. The lubrication difference between the two sides of AP-HC was further quantified by time-dependent friction tests. As shown in Figure 6F and G, the HC layer of AP-HC-2 exhibited a much lower COF than the AP layer, confirming that the hydration-rich HC surface provided effective lubrication. The lubricating stability of the HC side of AP-HC-2 was further evaluated under different applied loads, where it maintained a low and stable COF [Figure 6H]. The HC side of AP-HC-2 also preserved its lubricating behavior at 37 °C in physiologically relevant media, including PBS, serum, and PBS containing BSA [Figure 6I], suggesting tolerance to protein adsorption and complex biofluids. After immersion in water for up to 7 days, the lubricating performance remained stable [Figure 6J]. The HC gel exhibited gradual degradation in simulated body fluid at 37 °C, with a weight loss of approximately 36% after 7 days [Supplementary Figure 14A]. Despite this partial degradation, AP-HC maintained a low COF of approximately 0.05 after 48 h of immersion, indicating retained hydrated lubrication during physiological incubation [Supplementary Figure 14B]. To evaluate the durability of the HC lubricating layer, AP-HC-2 was evaluated using two independent friction tests: 30 min of continuous sliding and a separate 900-cycle friction test [Supplementary Figure 15]. The COF remained low and stable in both tests, while post-friction SEM images showed a continuous HC surface without obvious cracks or delamination, demonstrating the excellent lubrication durability and structural stability of the HC layer. The macroscopic effect of this low-friction surface was further demonstrated by weight-dragging tests and by pulling a PVC strip clamped between two AP-HC pieces [Figure 6K and Supplementary Figure 16]. In both cases, the HC side required a substantially lower pulling force than the adhesive AP side or the bare tabletop. Together, these results demonstrate that the interfacial integration strategy simultaneously achieves robust HC-layer retention and durable hydration lubrication, enabling the adhesive and lubricating functions to coexist stably within one Janus hydrogel platform.

Anti-biofouling performance, biocompatibility, and substrate adaptability

For biomedical interface materials, effective biofouling resistance is essential for minimizing nonspecific biological adhesion, tissue irritation, and long-term functional failure. The HC side of AP-HC was designed as a hydrated, cell-repellent interface; its anti-cell-adhesion behavior was evaluated using L929 mouse fibroblasts.

We further examined anti-cell-adhesion performance by fluorescence imaging after cell culture and PBS washing [Figure 7A and B]. Compared with the control and adhesive surface, only a small number of L929 cells remained on the HC side of AP-HC-2, indicating greatly reduced cell attachment. Quantitative analysis confirmed the significant decrease in adherent cell density, demonstrating that the HC layer functions as an effective cell-repellent surface. The protein adsorption assay in Figure 7C showed that the amount of protein adsorbed on the HC side of AP-HC-2 was significantly lower than that on PVC and AP-2, confirming the protein-resistant character of the hydrated HC surface [Supplementary Figure 17]. This result is consistent with the surface design of AP-HC: while the AP side provides wet adhesion for stable fixation, the exposed HC side resists biological adhesion through its hydrated polysaccharide-rich network. Therefore, the Janus architecture spatially separates stable attachment and antibiofouling behavior within one integrated material.

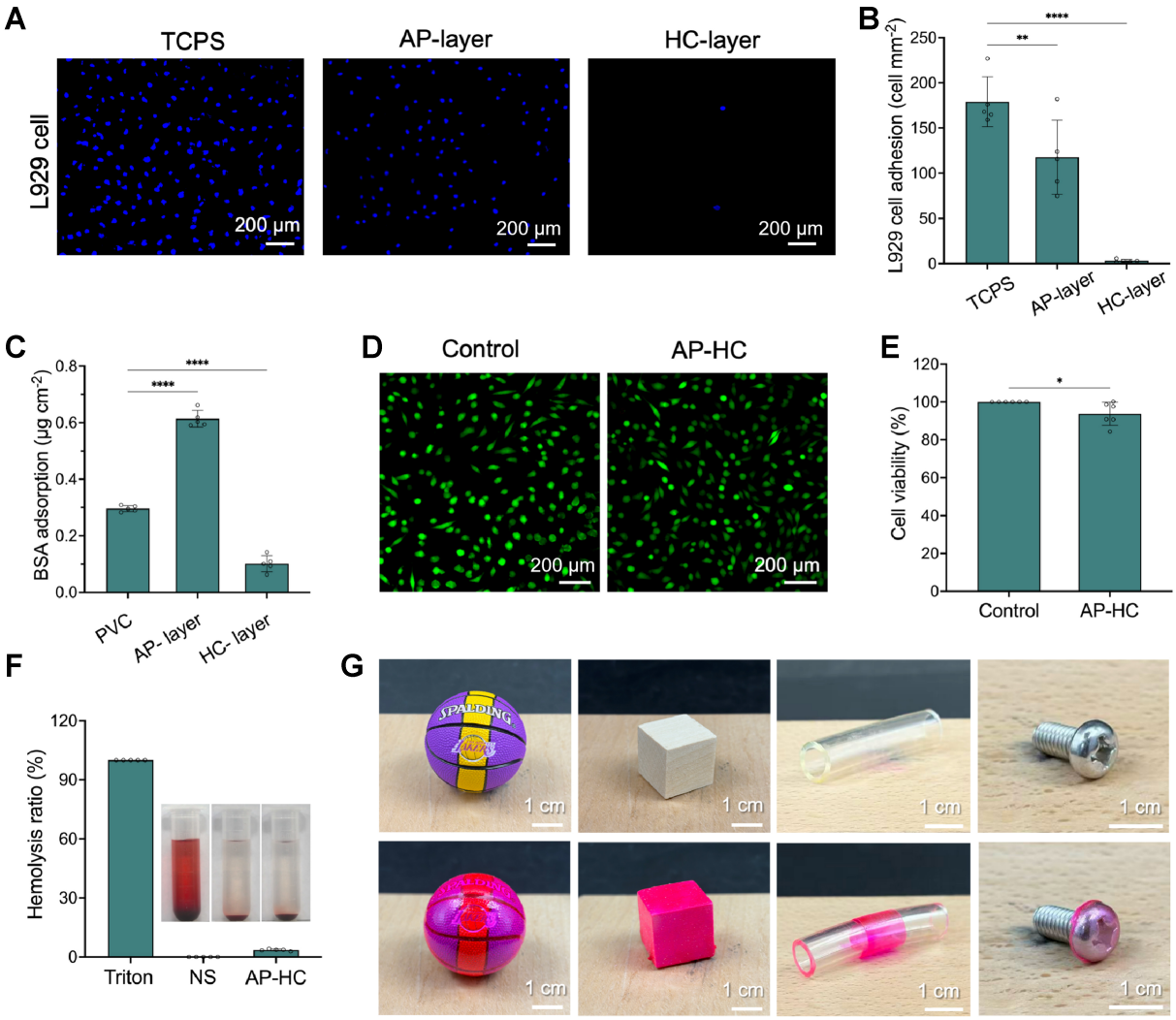


Figure 7. Anti-biofouling performance, biocompatibility, and substrate adaptability of the AP-HC bilayer hydrogel. (A and B) Fluorescence images of Hoechst 33342-stained L929 cells and corresponding quantitative analysis of cell adhesion on the hydrophilic surface of AP-HC-2; (C) Quantified BSA adsorption on PVC, AP-2, and the HC side of AP-HC-2, calculated from the standard curve and expressed as the amount of adsorbed protein per unit exposed surface area; (D and E) Calcein AM/PI fluorescence staining images and cell viability of L929 cells after 24 h of treatment with the AP-HC-2 extract prepared at an extraction ratio of 0.2 g·mL^{-1}; (F) Hemolysis ratio of AP-HC-2; (G) Photographs showing the conformal adhesion of the hydrogel coating on objects with different shapes and materials (The hydrogel was stained with Rhodamine B to improve visual contrast due to its high transparency). Data are presented as mean ± SD; n = 5 independent samples for (B), (C), and (F), and n = 6 independent samples for (E). $^{****}P < 0.0001$; $^{**}P < 0.01$, $^{*}P < 0.05$. BSA: Bovine serum albumin; PVC: polyvinyl chloride; AM: calcein-AM (calcein acetoxymethyl ester); PI: propidium iodide; SD: standard deviation; TCPS: tissue culture polystyrene; NS: normal saline.

The biological safety of AP-HC was assessed by cytocompatibility and hemocompatibility tests. Calcein-AM/PI staining showed that most L929 cells remained viable after 24 h of treatment with the AP-HC-2 extract, with abundant green fluorescence and limited red fluorescence [Figure 7D]. The cytocompatibility of extracts from AP-HC hydrogels with different AP/HC ratios is presented in Supplementary Figure 18. Cell viability remained above 90%, although a slight but statistically significant reduction was observed compared with the control group, indicating acceptable cytocompatibility of the AP-HC-2 hydrogel [Figure 7E]. The hemolysis ratio of AP-HC-2 was below 5% [Figure 7F], indicating acceptable blood compatibility. Beyond biological compatibility, practical device coating also requires adaptability to substrates with different geometries and compositions. As shown in Figure 7G, the hydrogel could stably conform to substrates with diverse shapes and materials, including a rubber ball, wooden block, plastic tube, and screw. This result

demonstrates its excellent shape and material adaptability, enabling intimate contact with curved, flat, and irregular surfaces. Such adaptability highlights its potential for the functional modification of medical devices with complex geometries. Collectively, these results demonstrate that AP-HC not only provides an effective antibiofouling HC interface, but also exhibits good cytocompatibility, hemocompatibility, and substrate adaptability, supporting its potential use as a safe Janus hydrogel platform for wet biomedical interfaces.

CONCLUSIONS

This work establishes a structure-defined design principle for reconciling the intrinsic antagonism between wet adhesion and hydrated lubrication within a single hydrogel interface. By spatially assigning wet adhesion and hydration-mediated lubrication/antifouling to the AP and HC sides, respectively, the AP-HC hydrogel achieves clear functional polarization while maintaining robust interlayer integration. This integration is attributed to interfacial precursor infiltration, polymer interdiffusion, and subsequent *in situ* crosslinking between the two hydrogel layers. This integrated interface not only mechanically couples the two functionally conflicting layers and enables pronounced functional polarization, but also allows AP-HC to maintain robust interlayer stability under prolonged aqueous exposure and dynamic perturbations. More broadly, this work provides a practical design principle for constructing multifunctional wet biointerfaces with robust interlayer coupling and spatially polarized surface functions, and this strategy may be extendable to other chemically compatible Janus hydrogel systems. Nevertheless, the present study is primarily focused on material design and *in vitro* evaluation, and the *in vivo* efficacy of AP-HC remains to be established. Future studies will therefore focus on evaluating its tissue-level biological responses, long-term interfacial stability, and functional performance under physiologically relevant conditions.

DECLARATIONS

Acknowledgements

Part of this work was conducted at Taiyuan University of Technology. We thank the Analytical and Testing Center of Taiyuan University of Technology for their support.

Authors' contributions

Conceptualized the study and designed the experiments: Yang, X.; Ye, Y. N.; Zhu, S.
Performed most of the experiments and analyzed the data: Yang, X.; Wang, Y.
Assisted with experiments and data collection: Zhang, Y.; Xu, Z.; Yang, C.; Ye, J.; Zhu, Y.
Assisted with the biological experiments: Hu, Y.; Guo, S.
Wrote the original draft: Yang, X.; Zhu, S.
Reviewed and edited the manuscript: Yang, X.; Ye, Y. N.; Zhu, S.
Supervised the research, provided resources and funding, and administered the project: Wang, H.; Ye, Y. N.; Zhu, S.
All authors reviewed and approved the final manuscript.

Availability of data and materials

The original contributions presented in this study are included in the article and Supplementary Materials. Please direct further inquiries to the corresponding authors.

AI and AI-assisted tools statement

Not applicable.

Financial support and sponsorship

This work was supported by the Young Scientists Fund of the National Natural Science Foundation of China (52303028), the Shanxi Provincial Youth Scientific Research Project (202503021212036), and the General Project of Shaanxi Province Research and Development Key Program [No. 2022NY-042].

Conflicts of interest

All authors declared that there are no conflicts of interest.

Ethical approval and consent to participate

Not applicable.

Consent for publication

Not applicable.

Copyright

© The Author(s) 2026.

Supplementary Materials

Supplementary Materials

REFERENCES

1. Liu, X.; Liu, J.; Lin, S.; Zhao, X. Hydrogel machines. *Mater. Today.* **2020**, *36*, 102-24. DOI
2. Yuk, H.; Lu, B.; Zhao, X. Hydrogel bioelectronics. *Chem. Soc. Rev.* **2019**, *48*, 1642-67. DOI PubMed
3. Yang, J.; Bai, R.; Chen, B.; Suo, Z. Hydrogel adhesion: a supramolecular synergy of chemistry, topology, and mechanics. *Adv. Funct. Mater.* **2020**, *30*, 1901693. DOI
4. Ullah, A.; Kim, D. Y.; Lim, S. I.; Lim, H. R. Hydrogel-based biointerfaces: recent advances, challenges, and future directions in human-machine integration. *Gels* **2025**, *11*, 232. DOI PubMed PMC
5. Lee, M. Y.; Lee, E. S.; Ko, N. Y.; et al. Emerging roles of hydrogels, organogels, and their hybrids in soft bioelectronics and bioplatforms. *npj. Biosens.* **2025**, *2*, 35. DOI
6. Chong, J.; Sung, C.; Nam, K. S.; et al. Highly conductive tissue-like hydrogel interface through template-directed assembly. *Nat. Commun.* **2023**, *14*, 2206. DOI PubMed PMC
7. Ren, X.; Zhang, J.; Yang, F.; Xu, H.; Guo, G.; Wang, Y. Enzyme-immobilized surface-catalyzed cross-linking: creating multifunctional double network hydrogel coatings on diverse substrates. *Adv. Funct. Mater.* **2024**, *34*, 2312465. DOI
8. Zhang, L.; Wang, L.; Li, W.; et al. Bioinspired hydrogels for enhanced wet adhesion: from natural mechanisms to biomedical applications. *Chem. Eng. J.* **2025**, *520*, 165878. DOI
9. Cui, C.; Liu, W. Recent advances in wet adhesives: adhesion mechanism, design principle and applications. *Prog. Polym. Sci.* **2021**, *116*, 101388. DOI
10. Fan, H.; Wang, J.; Gong, J. P. Barnacle cement proteins-inspired tough hydrogels with robust, long-lasting, and repeatable underwater adhesion. *Adv. Funct. Mater.* **2021**, *31*, 2009334. DOI
11. Sun, J. Y.; Zhao, X.; Illeperuma, W. R.; et al. Highly stretchable and tough hydrogels. *Nature* **2012**, *489*, 133-6. DOI PubMed PMC
12. Yuk, H.; Zhang, T.; Lin, S.; Parada, G. A.; Zhao, X. Tough bonding of hydrogels to diverse non-porous surfaces. *Nat. Mater.* **2016**, *15*, 190-6. DOI PubMed PMC
13. Gong, J.; Katsuyama, Y.; Kurokawa, T.; Osada, Y. Double-network hydrogels with extremely high mechanical strength. *Adv. Mater.* **2003**, *15*, 1155-8. DOI
14. Yao, M.; Wei, Z.; Li, J.; et al. Microgel reinforced zwitterionic hydrogel coating for blood-contacting biomedical devices. *Nat. Commun.* **2022**, *13*, 5339. DOI PubMed PMC
15. Li, C.; Zheng, H.; Zhang, X.; Pu, Z.; Li, D. Zwitterionic hydrogels and their biomedical applications: a review. *Chem. Synth.* **2024**, *4*, 17. DOI
16. Liu, L.; Hou, H.; Zhao, B.; et al. A Janus adhesive hydrogel via one-pot phase separation for wound healing. *Health. Eng.* **2024**. DOI
17. Liu, Y.; Li, M.; Zheng, Y.; et al. Hydrogel coatings on universal medical devices with water-responsive Janus adhesion and acidity-triggered transformation for adaptive antibacterial treatment and fluorescence diagnosis. *Chem. Eng. J.* **2024**, *481*, 148673. DOI
18. Li, J.; Wang, Z.; Yang, W.; et al. Bionic Janus hydrogel drives infected Achilles tendon regeneration via mechano-immune spatiotemporal steering. *Nat. Commun.* **2026**, *17*, 1805. DOI PubMed PMC
19. Liu, H.; Yao, X.; She, Y.; et al. Strain-invariant highly conductive Janus organogels for AI-assisted bioelectronics. *Matter* **2026**, *9*, 102666. DOI
20. Shao, H.; Deng, J.; Xu, Z.; et al. A Janus hydrogel that enables wet tissue adhesion and resists abdominal adhesions. *Mater. Today. Bio.* **2024**, *28*, 101248. DOI PubMed PMC
21. Yang, Y.; He, L.; Guan, G.; et al. Janus hydrogels: pioneering dual-faced biomaterials for revolutionary tissue engineering. *Mater. Today. Adv.* **2025**, *28*, 100652. DOI
22. Ouyang, C.; Shen, F.; Yu, H.; et al. Nanoscale phase separation induced self-reinforced Janus hydrogel achieves robust adhesion under extreme acidity and anti-postoperative adhesions. *J. Colloid. Interface. Sci.* **2026**, *707*, 139736. DOI PubMed

23. Gao, Y.; Guo, J.; Li, S.; et al. A bio-adaptive Janus-adhesive dressing with dynamic lubrication overlayer for prevention of postoperative infection and adhesion. *Adv. Sci.* **2025**, *12*, e2500138. DOI PubMed PMC
24. Zhang, Y.; Li, D.; Liu, M.; et al. An oral mucosa-inspired wet-adhesion Janus hydrogel with asymmetric bifunctionalities of antifouling/antioxidant for treating oral ulcer in diabetes. *Small* **2026**, *22*, e13928. DOI PubMed
25. Liu, H.; Liu, C.; Shao, D.; et al. A tough Janus hydrogel patch with strong wet adhesion and self-debonding for oral ulcer treatment. *Chem. Mater.* **2024**, *36*, 4976-89. DOI
26. Wang, X.; Wang, J.; Yu, Y.; et al. A polyzwitterion-based antifouling and flexible bilayer hydrogel coating. *Compos. Part. B. Eng.* **2022**, *244*, 110164. DOI
27. Sophia Fox, A. J.; Bedi, A.; Rodeo, S. A. The basic science of articular cartilage: structure, composition, and function. *Sports. Health.* **2009**, *1*, 461-8. DOI PubMed PMC
28. Yang, X.; Wang, H.; Yue, C.; et al. Polysaccharide-based hydrogel formed via in situ schiff base reaction with contact lens-like ocular surface coverage for sustained ophthalmic drug delivery. *Chin. J. Polym. Sci.* **2026**, *44*, 1804-19. DOI
29. Xu, Y.; Patsis, P. A.; Hauser, S.; et al. Cytocompatible, injectable, and electroconductive soft adhesives with hybrid covalent/noncovalent dynamic network. *Adv. Sci.* **2019**, *6*, 1802077. DOI PubMed PMC
30. Yuk, H.; Varela, C. E.; Nabzdyk, C. S.; et al. Dry double-sided tape for adhesion of wet tissues and devices. *Nature* **2019**, *575*, 169-74. DOI PubMed
31. Wang, H.; Wang, M.; Wu, J.; et al. Nature-inspired gelatin-based adhesive hydrogel: a rapid and user-friendly solution for hemostatic applications. *Adv. Healthc. Mater.* **2024**, *13*, e2304444. DOI PubMed
32. Quan, H.; Yang, W.; Lapeyriere, M.; Schaible, E.; Ritchie, R. O.; Meyers, M. A. Structure and mechanical adaptability of a modern elasmoid fish scale from the common carp. *Matter* **2020**, *3*, 842-63. DOI
33. Wei, L.; Song, L.; Yan, Y.; et al. Constructing of functional hydrogel coatings via combined surface laser ablation with surface-initiated polymerization. *Chem. Eng. J.* **2025**, *519*, 164906. DOI
34. Liu, J.; Shen, K.; Chu, D.; Cheng, Y. Tempo-functionalized Janus hydrogel crosslinked by tandem dynamic covalent bonds for internal organ injury repair and deep second-degree burn wound healing. *Adv. Funct. Mater.* **2025**, *35*, 2505194. DOI
35. Su, X.; Hao, D.; Li, J.; et al. A dynamically adaptive wet-adhesive Janus hydrogel patch for sutureless repair of spinal dural defects. *Bioact. Mater.* **2026**, *56*, 509-21. DOI PubMed PMC
36. Zhang, Y.; Liu, L.; Yu, X.; et al. A bio-inspired Janus hydrogel patch facilitates oral ulcer repair by combining prolonged wet adhesion and lubrication. *Acta. Biomater.* **2024**, *190*, 120-32. DOI PubMed
37. Bai, M. H.; Zhao, B.; Liu, Z. Y.; et al. Mucosa-like conformal hydrogel coating for aqueous lubrication. *Adv. Mater.* **2022**, *34*, e2108848. DOI PubMed
38. Illescas, J.; Ramirez-Fuentes, Y. S.; Rivera, E.; et al. Synthesis and optical characterization of photoactive poly(2-phenoxyethyl acrylate) copolymers containing azobenzene units, prepared by frontal polymerization using novel ionic liquids as initiators. *J. Polym. Sci. A. Polym. Chem.* **2012**, *50*, 821-30. DOI
39. Vijayanand, P. S.; Arunprasath, R.; Balaji, R.; Nanjundan, S. Synthesis, spectral properties, and thermal properties of homo- and copolymers of 3,5-dimethylphenyl acrylate with glycidyl methacrylate and determination of reactivity ratios. *J. Appl. Polym. Sci.* **2002**, *85*, 2261-70. DOI
40. Robins, J. H.; Abrams, G. D.; Pincock, J. A. The structure of Schiff reagent aldehyde adducts and the mechanism of the Schiff reaction as determined by nuclear magnetic resonance spectroscopy. *Can. J. Chem.* **1980**, *58*, 339-47. DOI
41. Karkantonis, T.; Gaddam, A.; Sharma, H.; Cummins, G.; See, T. L.; Dimov, S. Laser-enabled surface treatment of disposable endoscope lens with superior antifouling and optical properties. *Langmuir* **2022**, *38*, 11392-405. DOI PubMed PMC
42. Sunny, S.; Cheng, G.; Daniel, D.; et al. Transparent antifouling material for improved operative field visibility in endoscopy. *Proc. Natl. Acad. Sci. U. S. A.* **2016**, *113*, 11676-81. DOI PubMed PMC
43. Zhang, Y.; Feng, S.; Zhu, S.; et al. A bioinspired hydrogel with balanced adhesion and compliance for reversible underwater adhesion. *Mater. Chem. Front.* **2026**, *10*, 2152-61. DOI
44. Fan, H.; Wang, J.; Tao, Z.; et al. Adjacent cationic-aromatic sequences yield strong electrostatic adhesion of hydrogels in seawater. *Nat. Commun.* **2019**, *10*, 5127. DOI PubMed PMC
45. Liao, H.; Hu, S.; Yang, H.; et al. Data-driven de novo design of super-adhesive hydrogels. *Nature* **2025**, *644*, 89-95. DOI PubMed PMC

Disclaimer/Publisher's Note: All statements, opinions, and data contained in this publication are solely those of the individual author(s) and contributor(s) and do not necessarily reflect those of OAE and/or the editor(s). OAE and/or the editor(s) disclaim any responsibility for harm to persons or property resulting from the use of any ideas, methods, instructions, or products mentioned in the content.



© The Author(s) 2026. Open Access This article is licensed under a Creative Commons Attribution 4.0 International License (https://creativecommons.org/licenses/by/4.0/), which permits unrestricted use, sharing, adaptation, distribution and reproduction in any medium or format, for any purpose, even commercially, as long as you give appropriate credit to the original author(s) and the source, provide a link to the Creative Commons license, and indicate if changes were made.